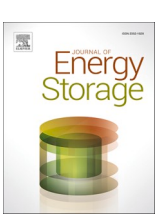
ELSEVIER

Contents lists available at ScienceDirect

Journal of Energy Storage

journal homepage: www.elsevier.com/locate/est



Research papers

Asymmetric variable flow-rate control enhances capacity and efficiency in vanadium redox flow batteries

Shaojin Wang ^a, Yana Zhou ^{a,*}, Yang Li ^{b,*}, Chengyan Li ^a, Xifeng Lin ^a, Xinan Zhang ^c, Binyu Xiong ^{a,d,*}

- ^a Wuhan University of Technology, Wuhan, China
- ^b School of Electrical Engineering and Automation, Wuhan University, Wuhan, China
- School of Engineering, The University of Western Australia, Australia
- ^d Hubei Province New Energy Power Battery Engineering Research Center, China

ARTICLE INFO

Keywords: Vanadium redox flow battery Asymmetric flow rate Electrolyte volume Control strategy Capacity degradation

ABSTRACT

Vanadium redox flow batteries (VRBs) are promising for large-scale energy storage, yet their long-term performance is often compromised by electrolyte volume imbalances induced by ion migration and self-discharge. Existing flow rate control strategies have primarily focused on enhancing system efficiency, often at the expense of capacity retention and system stability. In this work, we propose a novel flow control strategy that integrates asymmetric and variable flow-rate control strategies to dynamically counteract electrolyte migration during cycling. This asymmetrical variable flow-rate (AVF) strategy is supported by a high-fidelity VRB model developed based on Darcy's law, which characterizes electrolyte volume variations by incorporating the effects of viscosity, flow rate, and migrated electrolyte volume. With this model, a direct link is established between the state of charge and electrolyte viscosity. We then formulate and solve a constrained optimization problem using a heuristic approach to achieve adaptive flow regulation. Experimental validation demonstrates that the proposed AVF control strategy outperforms existing strategies by significantly reducing electrolyte migration, increasing discharge capacity, and slowing capacity degradation, which offers a practical pathway to enhance VRB longevity and efficiency.

1. Introduction

As demand for reliable and sustainable energy solutions grows, large-scale grid energy storage has become increasingly essential for integrating renewable energy sources. Among various storage technologies, vanadium redox flow batteries (VRBs) are recognized for their safety, scalability, and long lifespan. Over the past two decades, VRB technology has gained significant attention and progressed rapidly, driven by advancements in both research and industrial applications [1]. A VRB functions by utilizing a positive electrolyte containing VO^{2+} and VO^{2+} ions and a negative electrolyte containing V^{2+} and VO^{3+} ions. These redox-active species are dissolved in a dilute sulfuric acid solution and continuously circulated between storage tanks and the electrochemical stack, where reversible redox reactions facilitate energy storage and release [2]. For VRB systems, both efficiency and capacity are critical performance indicators. Efficiency directly affects the cost of operation by influencing cycle performance [3,4]. The capacity, on the other hand,

of the battery affects its long-term cyclability and the associated maintenance costs [5].

Various parasitic losses, including pump losses, self-discharge losses, electrochemical losses, and resistive losses, affect overall system efficiency. Electrochemical and resistive losses can be reduced by limiting concentration overpotentials and ohmic overpotentials, which are the focus of numerous studies, by improving key VRB components such as membrane [6], flow field [7], electrode structure [8], and stack [9,10]. Novel control strategies and internal state optimization techniques have been proposed to reduce pump losses, which represent the primary component of parasitic losses [11,12]. These strategies consider the electrolyte flow rate at which active materials are transported into the stack as a distinctive feature. Higher flow rates can reduce concentration overpotential and enhance voltage efficiency [13], but they can also increase pumping losses and lower system efficiency [14]. Early studies typically employed constant flow-rate (CF) control strategies, i.e., the fixed optimized flow rates are applied during operation and not subject to real-time adjustment. In order to balance the concentration

E-mail addresses: yanazhou@whut.edu.cn (Y. Zhou), yangli@ieee.org (Y. Li), bxiong2@whut.edu.cn (B. Xiong).

^{*} Corresponding authors.

Nomen	clature	m	membrane
		b	bipolar plate
E_0	nominal voltage	\boldsymbol{E}	electrolyte
N	number of cells in the stack	act	activation
R	resistance	con	concentration
R_u	universal gas constant	n	negative
i_0	exchange current density	\boldsymbol{p}	positive
\boldsymbol{A}	area	H^+	proton
T	temperature	e	electrode surface
z	number of electrons transferred	ec	electrode cross-sectional
\boldsymbol{F}	Faraday's constant	2	V^{2+} ion
c	concentration	3	V^{3+} ion
η	overpotential	4	VO ²⁺ ion
Q	flow rate	5	VO_2^+ ion
V	volume	V	total vanadium ion
U	voltage	ch	charge
I	current	dch	discharge
d	membrane thickness	the	theoretical
J	current density	opt	optimal
Q_0	initial flow rate	O_2	oxygen evolution
P_0	ambient pressure	H_2	hydrogen evolution
Δt	duration of each cycle	H ₂ SO ₄	sulfuric acid
K	Kozeny-carman constant	H_2O	water
P	pressure of the cell	2 -	
L	electrode length	Superscr	ipts
d_f	carbon fiber diameter	t	tank
k	diffusion coefficient	(i,0)	quantities of <i>i</i> in the <i>i</i> -H ₂ O having the same water activity
Q_m	rate of electrolyte transfer through the membrane		as that of the mixed solution
M	molar mass with bound water	c	cell
n	molar amount		
C	current discharging capacity	Abbrevio	
C_0	optimal discharging capacity	VRB	vanadium redox flow battery
P_{pump}	pump power	SOC	state of charge
$c_{\rm reac}^t$	reactant concentration in the electrolyte tanks	SOH	state of health
reac t	duration	OCV	open-circuit voltage
·	duration	CE	coulomb efficiency
Greek sy	ymbols	VE	voltage efficiency
κ	electrode permeability	EE	energy efficiency
μ	electrolyte viscosity	SE	system efficiency
ε	porosity	VTR	volume transfer ratio
ξ	positive and negative flow rate asymmetric coefficient	i-H ₂ O	binary solutions
λ	flow rate factor	FF	flow-rate factor
$\lambda_{1,opt}$	optimal flow rate factor of constant flow rate	CF	constant flow-rate
$\lambda_{2,\text{opt}}$	optimal flow rate factor of variable flow rate	VF	variable flow-rate
		ACF	asymmetrical constant flow-rate
Subscrip		AVF	asymmetrical variable flow-rate
ohm	ohmic		

overpotentials and pumping losses, more advanced flow control strategies have been proposed. For example, Prathak et al. [15] employed an extended Kalman filter to estimate vanadium ion concentrations. Based on these real-time estimates, the flow rate was dynamically adjusted, leading to a 7.4 % improvement in system efficiency. Ma et al. [16] proposed a strategy to optimize the flow rate at different stages of the charging and discharging processes, resulting in an 8 % increase in system efficiency compared to the conventional CF strategy, while maintaining high capacity. Tang et al. [17] defined the flow-rate factor (FF) and demonstrated through simulations that an FF of 7.5 yields the highest SE. Massimo et al. [18] conducted cycling experiments on a 9-kW/27-kWh VRB test platform, with results showing an increase of round-trip efficiency of around 2 % at an FF of 7.5. Subsequently, various works have expanded upon this concept, including the optimal FF strategy [19] and the online FF strategy based on multi-physical field

coupling [20]. Unfortunately, most of these studies have concentrated on efficiency improvements while disregarding changes in capacity, resulting in approaches that do not fully address the systemic challenges of balancing capacity and efficiency.

The long-term performance of VRB systems is influenced by several factors, including ion migration, self-discharge, bypass currents, gas release, and convection. These factors drive the migration of the electrolyte from the negative to the positive tanks, leading to volume imbalance and, ultimately, accelerating the degradation of battery capacity. To address this problem, various studies have focused on the optimized design of key components, such as electrode materials [21,22], membranes [21,23], and electrolytes [24,25]. Furthermore, many control strategies have been proposed to mitigate electrolyte imbalance. For example, Lu et al. [26] found that increases in the initial concentration of the cathode electrolyte and cathode outlet pressure can

inhibit the decay of battery discharge capacity. Toja et al. [27] successfully reduced the capacity decay from 47.7 % to 20.9 % by presetting the electrolyte concentration for both tanks. Wang et al. [28] developed a valence modulation strategy to minimize the crossover of V²⁺ ions, and their results demonstrated a 52.33 % increase in cumulative discharge capacity over 400 cycles. However, these works lack exploration of the electrolyte migration mechanism that limits the longterm discharge capacity and stability of VRBs. To overcome this problem, later studies [29,30] focused on reducing the effect of osmotic convection by utilizing asymmetric flow rates to reduce capacity losses. Recently, Song et al. [31] experimentally demonstrated that the pressure drop across the membrane is related to the viscosity difference. They proposed a method using positive and negative asymmetric flow rates to reduce the osmotic convection, resulting in a 1 % increase in available discharge capacity over 50 cycles. In another work [32], Fetyan et al. employed an asymmetric flow rate in a 50-cycle experiment, achieving a 5 % increase in discharge capacity and effectively mitigating electrolyte imbalance.

Although previous studies have provided valuable insights into electrolyte transfer behavior and potential methods to address capacity fade in VRBs, optimizing VRB performance considering more control objectives and practical constraints remains largely unexplored. The existing literature reviewed above offers various solutions to enhance VRB performance, particularly through detailed analyses of electrolyte migration mechanisms. On the one hand, while variable flow-rate (VF) control strategies have been proposed in several studies [17-19], the primary focus has been on optimizing FF configurations, with limited attention to broader performance objectives such as considering imbalance mitigation. On the other hand, although asymmetric flow rate strategies have been investigated [31,32], existing approaches rely on predetermined optimized flow rates that cannot be adjusted in real time. The lack of adaptability in these asymmetrical constant-flow (ACF) strategies limits the potential to significantly enhance the performance of VRBs, particularly in mitigating electrolyte crossover and extending system lifespan. Such limitation poses challenges in the practical deployment of VRBs in large-scale grid applications, where stable performance, durability, and reliability are crucial for economic viability.

To address this issue, this paper presents novel model-based heuristic control strategies by combining asymmetric and VF operations to enhance capacity retention and efficiency in VRBs. First, a dynamic model for electrolyte volume variation is developed using Darcy's law, and a comprehensive analysis of the underlying electrolyte transport mechanisms is conducted. The accuracy of this model is validated through experimental verification. Based on this model, we propose an asymmetric variable flow-rate (AVF) control strategy that dynamically adjusts the flow rates on two sides according to the changes in the state of charge (SOC) to counteract electrolyte migration. The feasibility and effectiveness of this strategy are evaluated by analyzing key performance indicators, including electrolyte volume variations, stack voltage, open-circuit voltage (OCV), and battery state of health (SOH). Experimental results confirm that the proposed AVF strategy significantly reduces electrolyte migration, enhances discharge capacity, and improves overall system performance.

The rest of this paper is organized as follows. Section 2 presents the governing equations of the VRB model and analyzes the mechanisms of electrolyte transfer. The proposed AVF control strategy is introduced in Section 3. In Section 4, the model is experimentally verified using a labscale VRB system. Simulation results and detailed discussions are provided in Section 5. Finally, the conclusions are summarized in Section 6.

2. Model development

The mathematical model development is based on the conservation of mass and charge, and the assumptions below are made to simplify the model without loss of generality:

- The stack and tank volumes on the positive and negative sides are identical.
- 2) An isothermal condition is assumed in the entire domain.
- 3) Viscosity changes of the positive and negative electrolytes due to battery aging are not taken into account.
- 4) The total internal resistance of the battery is assumed to be constant.
- 5) Vanadium ions are uniformly distributed throughout the electrolyte tanks and stack.

2.1. Governing equations of the VRB model

The OCV of VRB, E_{ocv} , is derived from the Nernst equation:

$$E_{\text{ocv}} = E_0 + \frac{R_u T}{zF} \ln \left(\frac{c_4^c \cdot c_5^c \cdot c_{\text{H}^+}^c}{c_5^c \cdot c_3^c} \right)$$
 (1)

where E_0 is the nominal voltage, R_u is the universal gas constant, T is the temperature, z is the number of electrons transferred in a redox reaction, and F is Faraday's constant. Furthermore, c_i^c (i=2,3,4, and 5) and c_{H^+} represent the concentrations of species V^{2+} , V^{3+} , VO^{2+} , VO^+_2 , and V^{2+} in the cell, respectively.

The voltage U_{stack} of the stack is expressed based on a circuit model [20]:

$$U_{\text{stack}} = N(E_{\text{ocv}} + \eta_{\text{ohm}} + \eta_{\text{act}} + \eta_{\text{con}})$$
 (2)

where N is the number of cells in the stack, $\eta_{\rm ohm}$ is the ohmic overpotential, $\eta_{\rm act}$ is the activation overpotential, and $\eta_{\rm con}$ is the concentration overpotential. These overpotentials are calculated by

$$\eta_{\rm ohm} = I(R_b + R_m + R_E) = IR_{\rm ohm} \tag{3}$$

$$\eta_{\rm act} = \frac{2R_u T}{zF} \ln \left(\frac{i_0}{I/A_a} \right) \tag{4}$$

$$\eta_{\rm con} = \frac{R_u T}{zF} \ln \left(1 - \frac{I}{1.6 \times 10^{-4} \times zFQc_{\rm reac}^t} \right)$$
 (5)

where I is the battery current. In (3), $R_{\rm ohm}$ is the ohmic resistance. It consists of three components: R_b , R_m , and R_E , which represent the resistances of the bipolar plate, membrane, and electrolyte, respectively. In (4), i_0 is the exchange current density on the electrode surface, and $A_{\rm e}$ represents the electrode surface area. Due to the large surface area of the porous electrode as the electrode material in VRB, $\eta_{\rm act}$ can be ignored [20]. In (5), $c_{\rm reac}^t$ is the reactant concentration in the electrolyte tanks. Q represents the flow rate and is the average of the flow rates on both the positive and negative sides.

Vanadium ions in the four oxidation states undergo redox reactions at positive and negative electrolytes to store and release electrical energy [33]. Previous research [34] described the dynamic properties of vanadium ions based on first principles, which include charge conservation and mass conservation. This modeling approach is also adopted in the present study. Unlike previous works, however, we also account for the side reaction of gas release, which provides a more

comprehensive perspective on the variation in vanadium ion concentration. The governing equations are given as

$$\frac{V_{\text{c}}}{2} \cdot \frac{dc_2^c}{dt} = \underbrace{\frac{\textit{NJA}_e}{\textit{zF}}}_{redox} + \underbrace{\left(-\frac{k_2c_2^c}{d} - \frac{k_4c_4^c}{d} - \frac{2k_5c_5^c}{d}\right) \textit{NA}_m}_{crossover, self-discharge} - \underbrace{\frac{\textit{NI}_{shunt}}{\textit{zF}}}_{shunt \ current} - \underbrace{\frac{2P_0}{\textit{R}_u T} \frac{dV_{\text{H2}}}{dt}}_{gas \ evolutions} + \underbrace{Q_n\left(c_2^t - c_2^c\right)}_{convection}$$

$$\frac{V_{c}}{2} \frac{dc_{3}^{c}}{dt} = -\underbrace{\frac{NJA_{e}}{zF}}_{\text{redox}} + \underbrace{\left(-\frac{k_{3}c_{3}^{c}}{d} + \frac{2k_{4}c_{4}^{c}}{d} + \frac{3k_{5}c_{5}^{c}}{d}\right)NA_{m}}_{\text{crossover,self-discharge}} + \underbrace{\frac{NI_{\text{shunt}}}{zF}}_{\text{shunt current}} + \underbrace{\frac{2P_{0}}{R_{u}T} \frac{dV_{\text{H}_{2}}}{dt}}_{\text{convection}} + \underbrace{Q_{n}(c_{3}^{t} - c_{3}^{c})}_{\text{convection}} \tag{7}$$

$$\frac{V_{c}}{2} \cdot \frac{dc_{4}^{c}}{dt} = -\underbrace{\frac{NJA_{e}}{zF}}_{\text{redox}} + \underbrace{\left(-\frac{k_{4}c_{4}^{c}}{d} + \frac{3k_{2}c_{2}^{c}}{d} + \frac{2k_{3}c_{3}^{c}}{d}\right)NA_{m}}_{\text{crossover,self-discharge}} + \underbrace{\frac{NI_{\text{shunt}}}{zF}}_{\text{shunt current}} + \underbrace{\frac{4P_{0}}{R_{u}T} \cdot \frac{dV_{O_{2}}}{dt}}_{\text{gas evolutions}} + \underbrace{Q_{p}\left(c_{4}^{t} - c_{4}^{c}\right)}_{\text{convection}}$$
(8)

$$\frac{V_{c}}{2} \cdot \frac{dc_{5}^{c}}{dt} = \underbrace{\frac{NJA_{e}}{zF}}_{redox} + \underbrace{\left(-\frac{k_{5}c_{5}^{c}}{d} - \frac{2k_{2}c_{2}^{c}}{d} - \frac{k_{3}c_{3}^{c}}{d}\right)NA_{m}}_{crossover,self-discharge} - \underbrace{\frac{NI_{shunt}}{zF}}_{shunt \ current} - \underbrace{\frac{4P_{0}}{R_{u}T}\frac{dV_{O_{2}}}{dt}}_{gas \ evolutions} + \underbrace{Q_{p}\left(c_{5}^{t} - c_{5}^{c}\right)}_{convection}$$

where c_i and k_i (i=2,3,4, and 5) represent the concentration and the diffusion coefficient of the vanadium ions, V is the volume, $J=I/A_e$ denotes the current density, $I_{\rm shunt}$ represents the shunt current, d indicates the membrane thickness, A_m is the membrane area, and P_0 is the ambient pressure. Furthermore, the superscripts c and t represent the cell and tank, respectively, and the subscripts n, p, O_2 , and O_2 are represent the negative side, the positive side, hydrogen evolution, and oxygen evolution, respectively.

For (6)–(9), the left-hand side of the equations represents the change of vanadium-ion concentration. The first term on the right-hand side accounts for the effects of the redox reactions. The second term captures the impact of ion crossover and side reactions. The third term represents the influence of shunt currents on vanadium-ion concentrations. However, since our study employs a single-cell VRB, the effect of shunt currents can be neglected. The fourth term corresponds to gas-evolution effects. No gas is detected in long-term experiments; this term is also omitted. Finally, the fifth term describes the impact of electrolyte flow rate on changes in vanadium-ion concentration.

Gas evolution reactions are primarily induced by overcharging, electrode polarization, and limitations in reaction kinetics. When the electrode potential increases beyond the thermodynamic potential for water oxidation (1.23 V), oxygen gas is generated at the positive

Table 1
Chemical reactions in a VRB.

Reactions in the cell		Chemical equation, standard electrode potential		
Negative electrode	Redox Gas	V^{2+} $\rightleftarrows_{charge}^{discharge} V^{3+} + e^-, -0.26 \text{ V}$ $2H^+ + 2e^- \rightarrow H_2, 0 \text{ V}$		
	evolution			
Positive electrode	Redox	$VO_2^+ + 2H^+ + e^- \rightleftharpoons_{charge}^{discharge} VO^{2+} + H_2O, 1 V$		
	Gas evolution	$2H_2O \rightarrow O_2 + 4H^+ + 4e^-, 1.23 \text{ V}$		

electrode. Conversely, when the electrode potential drops below the reduction potential of protons (0 V), hydrogen gas is evolved at the negative electrode. Table 1 summarizes the redox and gas evolution reactions in VRBs.

As shown in Table 1, the generation of 1 mol of $\rm H_2$ consumes 2 mol of electrons, corresponding to a charge of 2F. Similarly, the formation of 1 mol of $\rm O_2$ requires 4 mol of electrons, equivalent to 4F. In the expression describing the variation in vanadium ion concentration, the molar amount of hydrogen and oxygen generated per unit time, denoted as $n_{\rm H_2}$ and $n_{\rm O_2}$, is calculated as follows [35]:

$$\frac{dn_{H_2}}{dt} = \frac{J_{H_2}A_e}{2F}$$
 (10)

$$\frac{dn_{O_2}}{dt} = \frac{J_{O_2} A_e}{4F} \tag{11}$$

The ideal state gas equation is:

(6)

(9)

$$P_0V = nR_uT \tag{12}$$

where P_0 represents the ambient pressure and V is the gas volume. According to (12), the relationship between n and V can be derived:

$$n_{H_2/O_2} = \frac{P_0 V_{H_2/O_2}}{R_u T} \tag{13}$$

By substituting (13) into (10) and (11), respectively, we obtain:

$$\frac{P_0}{R_u T} \frac{dV_{H_2}}{dt} = \frac{J_{H_2} A_e}{2F} \tag{14}$$

$$\frac{P_0}{R_u T} \frac{dV_{O_2}}{dt} = \frac{J_{O_2} A_e}{4F} \tag{15}$$

The vanadium ion concentration losses caused by gas evolution are given by:

$$\left(\frac{dc_2^c}{dt}\right)_{H_2} = -\frac{J_{H_2}A_e}{F} = -\frac{2P_0}{R_uT} \cdot \frac{dV_{H_2}}{dt}$$
 (16)

$$\left(\frac{dc_3^c}{dt}\right)_{H_-} = \frac{J_{H_2}A_e}{F} = \frac{2P_0}{R_uT}\frac{dV_{H_2}}{dt}$$
(17)

$$\left(\frac{dc_4^c}{dt}\right)_{O_2} = \frac{J_{O_2}A_e}{F} = \frac{4P_0}{R_uT} \frac{dV_{O_2}}{dt}$$
(18)

$$\left(\frac{dc_5^c}{dt}\right)_{O_0} = -\frac{J_{O_2}A_e}{F} = -\frac{4P_0}{R_u T}\frac{dV_{O_2}}{dt}$$
 (19)

During hydrogen evolution at the negative electrode, the generation of 1 mol of $\rm H_2$ consumes 2 mol of electrons. This reduces the number of electrons available for the reduction of V^{3+} to V^{2+} , thereby weakening the discharge reaction. As a result, the concentration of V^{3+} increases while that of V^{2+} decreases. Consequently, the coefficient of the $\rm H_2$ evolution term is -1 in the V^{2+} concentration expression and + 1 in the V^{3+} concentration expression.

Similarly, during oxygen evolution at the positive electrode, the formation of 1 mol of oxygen releases 4 mol of electrons. This increases the number of electrons available for the oxidation of VO^{2+} to VO_2^+ , thereby enhancing the discharge reaction at the positive electrode. As a result, the concentration of VO^{2+} increases, and that of VO_2^+ decreases. Therefore, the coefficient of the oxygen evolution term is +1 in the VO^{2+} concentration expression and -1 in the VO_2^+ concentration expression.

In the paper, the SOH and SOC of a VRB are defined as follows:

$$SOH = \frac{C_i}{C_0} = \frac{\int_0^{T_{i,\text{dch}}} I_{\text{dch}} dt}{\int_0^{T_{0,\text{dch}}} I_{\text{dch}} dt}$$
 (20)

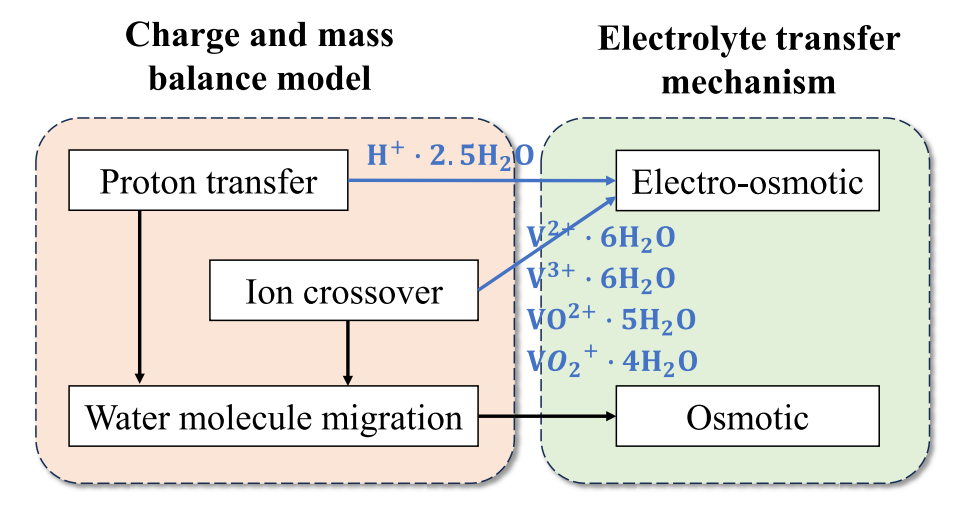


Fig. 1. Causes and mechanisms contributing to electrolyte volume change.

$$SOC = \min\left(\frac{c_2^t}{c_2^t + c_5^t}, \frac{c_5^t}{c_4^t + c_5^t}\right)$$
 (21)

where C_i and $T_{i,\rm dch}$ are the discharging capacity and duration in the *i*th cycle, C_0 and $T_{0,\rm dch}$ denote the initial discharging capacity and initial discharging duration, respectively, and $I_{\rm dch}$ is the discharge current.

2.2. Mechanism of electrolyte migration

Understanding the mechanisms driving electrolyte migration is essential for developing an effective flow rate control strategy that can enhance battery performance. All the causes and mechanisms contributing to electrolyte volume change are illustrated in Fig. 1. In the charge and mass balance model, the factors causing electrolyte volume change include proton transfer, ion crossover, and water molecule migration [36]. Proton transfer and ion crossover are both influenced by electric field-driven electro-osmotic forces [34]. Under the forces, protons cross the membrane alongside 2.5 H₂O molecules per proton [37]. Vanadium ions also diffuse through the membrane, carrying hydration shells that depend on their oxidation state (V2+.6H2O, V3+.6H2O, VO2+.5H2O, and VO₂⁺·4H₂O) [38]. Concurrently, proton transfer and ion crossover establish concentration gradients across the membrane, which in turn drive water migration via osmotic pressure [34]. Previous experimental [31] studies have demonstrated that electro-osmotic drag results in negligible net volume migration over long-term cycling. Consequently, osmotic pressure becomes the dominant cause of cumulative electrolyte transfer from the negative to the positive tanks during prolonged operation.

The water molecules are transferred against the concentration gradient due to osmotic pressure [39]. The electrolyte gradually migrates from the negative side to the positive side during long-term operation. As the positive and negative electrolyte imbalances worsen, the usable capacity of the VRB becomes limited by the negative half-cell, which results in a reduction of cycle life and deterioration of the battery's performance. The volume of the migrated electrolyte from the negative to the positive side is calculated as:

$$|\Delta V| = \Delta V_p = -\Delta V_n = Q_m \Delta t \tag{22}$$

where Q_m is the rate of electrolyte transfer through the membrane and Δt is the duration of each cycle. During charging–discharging cycling, a driving force persistently induces convective transport of water across

the membrane from the negative to the positive side. As a result, the usable capacity of the VRB becomes limited by the depletion of electrolyte on the negative side. Considering that the membrane is essentially a porous medium [31], based on Darcy's law, Q_m can be expressed as

$$Q_m = \frac{\kappa_m A_m}{\mu_n d} \left(P_n - P_p \right) \tag{23}$$

where κ_m is the membrane permeability, μ_n is the viscosity of the negative electrolyte, and P_n and P_p are the pressures of the negative and positive cells, respectively. Electrolyte migration is strongly influenced by the pressure differential between the positive and negative half-cells. Due to the presence of porous electrodes, Darcy's law remains applicable for each half-cell. The outlet pressure is approximately zero (i.e., standard atmospheric pressure of 101.3 kPa). Consequently, the average pressure in each half-cell can be considered to be half the inlet pressure:

$$P_n = \frac{\mu_n L Q_n}{2\kappa A_{\rm ec}} \tag{24}$$

$$P_p = \frac{\mu_p L Q_p}{2\kappa A_{ec}} \tag{25}$$

where $A_{\rm ec}$ is the electrode cross-sectional area, L is the electrode length, and κ is the electrode permeability, calculated by

$$\kappa = \frac{d_f^2}{K} \frac{\varepsilon^2}{(1 - \varepsilon)^2} \tag{26}$$

where d_f is the carbon fiber diameter, K is the Kozeny-Carman constant, and ε is the porosity of the porous medium.

Substituting (23)–(25) into (22) yields the expression of volume migration:

$$|\Delta V| = \Delta V_p = \frac{\kappa_m A_m}{\mu_n d} \cdot \frac{L}{2\kappa A_{\rm ec}} \left(Q_n \mu_n - Q_p \mu_p \right) \Delta t \tag{27}$$

3. Asymmetric variable flow-rate control strategy

3.1. Control objective and constraints

The fundamental premise underlying the prediction of electrolyte viscosity is to employ the viscosities of i-H₂O (binary solutions) that

constitute the VRB electrolyte. It has been shown that the viscosity of both the positive and negative electrolytes is correlated with the state of charge (SOC) of the battery [40], as described by

where M is the molar mass with bound water, and the subscripts V, H_2SO_4 , and H_2O represent total vanadium ion, sulfuric acid, and water,

$$\begin{split} \ln & \mu_n = \frac{M_2}{M_2^{(i.0)}} \cdot \ln \left(\left(1.362 + 0.215 \times c_V \times \text{SOC} + \right. \right. \\ & \left. \frac{M_2}{M_3^{(i.0)}} \cdot \ln \left(\left(1.913 - 0.855 \times c_V \times (1 - \text{SOC}) + \right. \right. \\ & \left. 1.05 \times (c_V \times (1 - \text{SOC}))^2 \right) \middle/ 1000 \right) + \\ & \left. \frac{M_{\text{H}_2\text{SO}_4}}{M_{\text{H}_2\text{SO}_4}^{(i.0)}} \cdot \ln \left(\left(0.941 + 0.144 \times \left(c_{\text{H}_2\text{SO}_4} + c_V \times 0.5 \times \text{SOC} \right) + \right. \right. \\ & \left. \left. 0.025 \times \left(c_{\text{H}_2\text{SO}_4} + c_V \times 0.5 \times \text{SOC} \right)^2 \right) \middle/ 1000 \right) + \\ & \left. \frac{M_{\text{H}_2\text{O}}}{M_{\text{H}_2\text{O}}^{(i.0)}} \cdot \ln \mu_{\text{H}_2\text{O}} \right. \end{split}$$

$$0.15 \times (c_V \times SOC)^2 / 1000 +$$
(28)

$$\begin{split} \ln & \mu_p = \frac{M_5}{M_5^{(i,0)}} \cdot \ln \Bigg(\Bigg(2.875 - 0.45 \times c_V \times \text{SOC} + \\ & \frac{M_4}{M_4^{(i,0)}} \cdot \ln \Bigg(\Bigg(2.751 + 1.61 \times c_V \times (1 - \text{SOC}) + \\ & 2.05 \times (c_V \times (1 - \text{SOC}))^2 \Bigg) \bigg/ 1000 \Bigg) + \\ & \frac{M_{\text{H}_2\text{SO}_4}}{M_{\text{H}_2\text{SO}_4}^{(i,0)}} \cdot \ln \Bigg(\Bigg(0.941 + 0.144 \times \big(c_{\text{H}_2\text{SO}_4} + c_V \times 0.5 \times \text{SOC} \big) + \\ & 0.025 \times \big(c_{\text{H}_2\text{SO}_4} + c_V \times 0.5 \times \text{SOC} \big)^2 \Bigg) \bigg/ 1000 \Bigg) + \\ & \frac{M_{\text{H}_2\text{O}}}{M_{\text{H}_2\text{O}}^{(i,0)}} \cdot \ln \mu_{\text{H}_2\text{O}} \\ & \frac{M_{\text{H}_2\text{O}}}{M_{\text{H}_2\text{O}}^{(i,0)}} \cdot \ln \mu_{\text{H}_2\text{O}} \end{aligned}$$

$$1.51 \times (c_V \times SOC)^2 \Big) \Big/ 1000 \Big) +$$
(29)

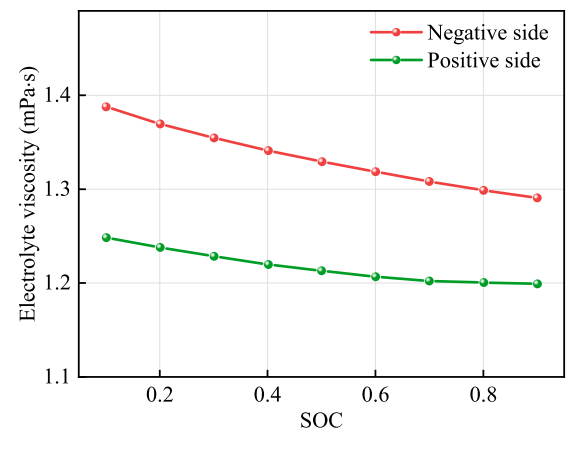


Fig. 2. Relationship between electrolyte viscosity μ and SOC in the positive and negative half-cells [40].

respectively. The superscript (i,0) indicates the quantities of i in the i-H₂O having the same water activity as that of the mixed solution [40]. The resulting relationships between the viscosity and SOC are expressed as two nonlinear functions, denoted by $\mu_n = f_n(\mathrm{SOC})$ and $\mu_p = f_p(\mathrm{SOC})$ as illustrated in Fig. 2.

Considering these relationships, (27) can be written as:

$$|\Delta V| = \frac{\kappa_m A_m L}{2d\kappa A_{ec}} \cdot \frac{1}{f_n(\text{SOC})} \left[Q_n f_n(\text{SOC}) - Q_p f_p(\text{SOC}) \right] \Delta t \tag{30}$$

By defining $\xi=Q_p/Q_n$ as the asymmetric coefficient, (30) can be rewritten as

$$|\Delta V| = \frac{\kappa_m A_m L}{2d\kappa A_{ec}} \cdot Q_n \left[1 - \xi \frac{f_p(SOC)}{f_n(SOC)} \right] \Delta t$$
 (31)

It can be seen that, for a given SOC, the volume migration becomes zero if the flow rate ratio is maintained as

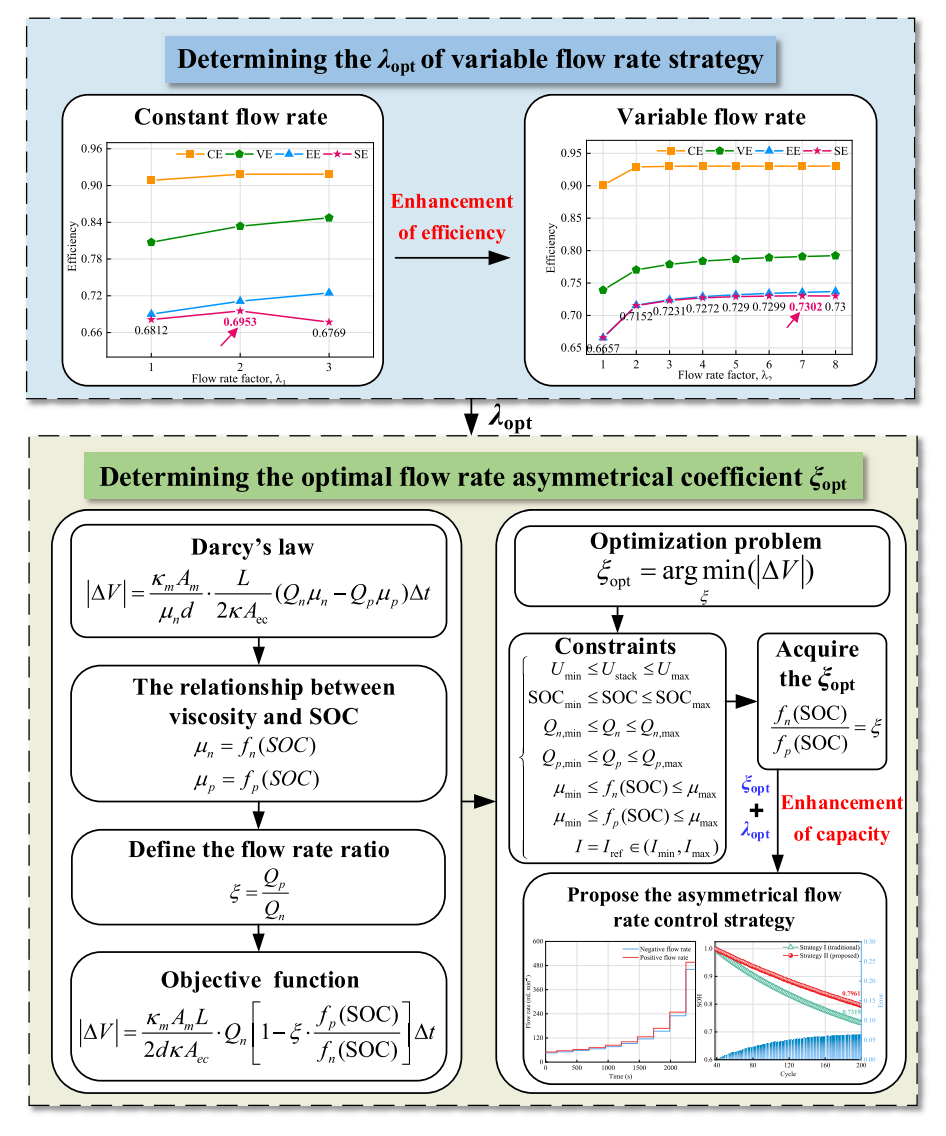


Fig. 3. Framework of the proposed control strategy of VRB systems.

$$\xi = \xi_{\text{opt}} = \frac{f_n(\text{SOC})}{f_p(\text{SOC})}$$
 (32)

The optimal flow rate ratio ξ_{opt} , for a given SOC, is determined by solving the following optimization problem:

$$\xi_{\rm opt} = \underset{\boldsymbol{\xi}}{\operatorname{argmin}}(|\Delta \boldsymbol{V}|) \tag{33}$$

subject to

$$\begin{cases} U_{\min} \leq U_{\text{stack}} \leq U_{\max} \\ \text{SOC}_{\min} \leq \text{SOC} \leq \text{SOC}_{\max} \\ Q_{n,\min} \leq Q_n \leq Q_{n,\max} \\ Q_{p,\min} \leq Q_p \leq Q_{p,\max} \\ \mu_{\min} \leq f_n(\text{SOC}) \leq \mu_{\max} \\ \mu_{\min} \leq f_p(\text{SOC}) \leq \mu_{\max} \\ I = I_{\text{ref}} \in (I_{\min}, I_{\max}) \end{cases}$$
(34)

where the maximum and minimum limits in the constraints are determined by specification and physical properties of the VRB.

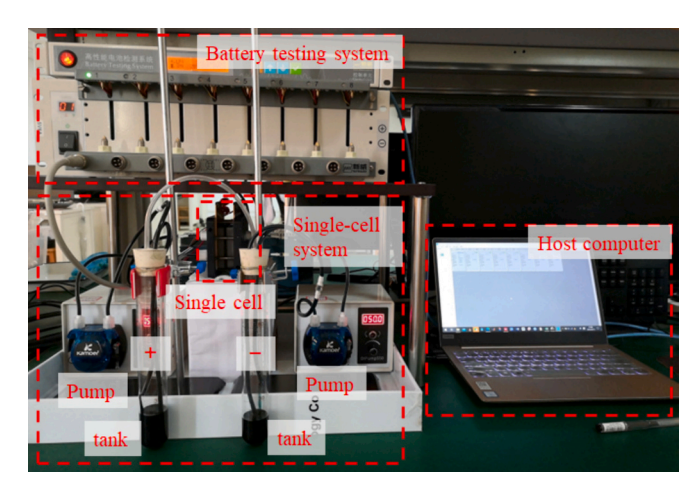


Fig. 4. A single-cell VRB experiment platform.

3.2. Control framework

VRB systems are conventionally controlled to maintain a CF calculated by

$$Q = \lambda \cdot Q_{\text{the}} = \lambda \cdot \frac{I}{zFc_V} \tag{35}$$

where Q_{the} is the theoretical minimum flow rate to maintain VRB system operation, λ is called the *flow-rate factor* (FF), and c_V is the total vanadium concentration.

To enhance system efficiency, we propose the AVF strategy to allow asymmetrical adjustment of the flow rates when the SOC changes, expressed by

$$Q = \lambda \cdot Q'_{\text{the}} = \begin{cases} \lambda \cdot \frac{I}{zFc_V(1 - \text{SOC})}, & \text{charging} \\ \lambda \cdot \frac{I}{zFc_V\text{SOC}}, & \text{discharging} \end{cases}$$
(36)

where Q'_{the} replaces the fixed Q_{the} as a function of SOC and the charging/discharging modes.

To implement this proposed algorithm, our control framework is structured with two main stages, as illustrated in Fig. 3. At Stage 1, given the measured or estimated SOC, we determine the corresponding optimal λ (denoted by λ_{opt}) of the AVF strategy. This λ_{opt} provides the reference flow rate for Stage 2.

Stage 1 is described as the following steps:

Step 1.1: Obtain the initial SOC (SOC $_0$), charging/discharging current $I_{\mathrm{ch/dch}}$, and T;

Table 2
Parameters of the VRB model.

Parameter	Value	Unit	Remark
Nominal voltage, E_0	1.412	V	_
Ohmic resistance, $R_{\rm ohm}$	0.035	Ω	Preset
Ambient pressure, P_0	101,325	Pa	-
Total vanadium concentration, C_V	1.5	$\mathrm{mol}{\cdot}\mathrm{L}^{-1}$	Preset
Electrolyte volume in each electrolyte tank, V_t	20	mL	Preset
Temperature, T	298.15	K	Preset
Cell volume, V_c	20	mL	Preset
Universal gas constant, R_u	8.314	J. (mol·K) ⁻¹	Preset
Faraday's constant, F	96,485	C·mol ⁻¹	Preset
Number of cells, N	1	_	Preset
Number of electrons transferred during	1	_	Preset
the reaction, z			
Current density, J	2000	$A \cdot m^{-2}$	Preset
Diffusion coefficient of V^{2+} , k_2	8.8×10^{-12}	$m^2 \cdot s^{-1}$	Preset
Diffusion coefficient of V^{3+} , k_3	3.2×10^{-12}	$m^2 \cdot s^{-1}$	Preset
Diffusion coefficient of VO^{2+} , k_4	6.8×10^{-12}	$m^2 \cdot s^{-1}$	Preset
Diffusion coefficient of VO_2^+ , k_5	5.9×10^{-12}	$m^2 \cdot s^{-1}$	Preset
Molar mass of V ²⁺ particles with bound	-6.7×10^{-2}	$kg \cdot mol^{-1}$	[34,36]
water, M ₂		1	
Molar mass of V^{3+} particles with bound water, M_3	$^{-2.1~\times}_{10^{-2}}$	kg·mol ^{−1}	[34,36]
Molar mass of VO^{2+} particles with bound water, M_4	-6.5×10^{-2}	$kg \cdot mol^{-1}$	[34,36]
Molar mass of VO_2^+ particles with bound	-1.09 ×	$kg \cdot mol^{-1}$	[34,36]
water, M_5	10^{-1}	Kg·IIIOI	[34,30]
Hydraulic permeability of the membrane, κ_m	1.58×10^{-18}	m^2	[36]
Effective membrane area, A_m	9×10^{-4}	m^2	Preset
Membrane thickness, d	1.25×10^{-4}	m	Preset
Electrode length, L	0.03	m	Preset
Electrode cross-sectional area, $A_{\rm ec}$	7.2×10^{-5}	m^2	Preset
Electrode surface area, A_e	9×10^{-4}	m^2	Preset
Carbon fiber diameter, d_f	1.76×10^{-5}	m	[41]
Kozeny–Carman constant, K	4.28	-	[17]
Electrode porosity, ε	0.93	-	[17]

Step 1.2: Obtain the initial theoretical minimum flow rate Q'_{the} of the AVF strategy;

Step 1.3: Calculate the coulombic efficiency (CE), voltage efficiency (VE), energy efficiency (EE), and system efficiency (SE) for AVFs during the last aging cycle. They are calculated by:

$$CE = \frac{\int_0^{t_{\rm dch}} I_{\rm dch} dt}{\int_0^{t_{\rm ch}} I_{\rm ch} dt}$$
(37)

$$VE = \frac{\int_0^{t_{dch}} U_{dch} dt}{\int_0^{t_{ch}} U_{ch} dt}$$
(38)

$$EE = \frac{\int_{0}^{t_{\rm dch}} U_{\rm dch} I_{\rm dch} dt}{\int_{0}^{t_{\rm ch}} U_{\rm ch} I_{\rm ch} dt}$$
(39)

$$SE = \frac{\int_0^{t_{dch}} (U_{dch}I_{dch} - P_{pump})dt}{\int_0^{t_{ch}} (U_{ch}I_{ch} + P_{pump})dt}$$
(40)

where the subscripts dch and ch represent the discharging and charging, respectively, U and I are the battery voltage (i.e., $U_{\rm stack}$) and current, respectively, t is the duration, and $P_{\rm pump}$ is the pump power and is a function of Q, calculated by:

$$P_{pump} = \frac{P_{pump,n}(Q_n) + P_{pump,p}(Q_p)}{2}$$
(41)

where $P_{\text{pump},n}$ and $P_{\text{pump},p}$ denote the consumed power by the negative and the positive pumps, respectively.

Step 1.4: λ_{opt} of the AVF strategy is obtained based on the SE performance.

Stage 2 involves the following steps:

Step 2.1: Given the SOC, calculate the variation of positive and negative electrolyte viscosity using $\mu_n=f_n({\rm SOC})$ and $\mu_p=f_p({\rm SOC})$;

Step 2.2: Calculate
$$F(SOC) = 1 - \xi \frac{f_p(SOC)}{f_n(SOC)}$$
 at different SOCs;

Step 2.3: Based on (32), obtain the variation of ξ with SOC;

Step 2.4: Based on ξ at different SOCs, obtain F(SOC) at different SOCs;

Step 2.5: Solve (33) and (34) for ξ_{opt} at different SOCs;

Optimal flow rate control can be achieved with the calculated values $\xi_{\rm opt}$ and $\lambda_{\rm opt}$.

4. Model validation

A lab-scale VRB experimental platform, shown in Fig. 4, is constructed and used to validate the proposed model. The platform consists of a single-cell VRB system (Wuhan Zhisheng New Energy Co., Ltd.), a battery testing system, and a host computer (Neware BTS 7.6X). The single-cell VRB system consists of a VRB stack, two electrolyte tanks, and two peristaltic pumps.

The VRB system operates at ambient temperature (298.15 K). It employs an Nafion 115 membrane, with its diffusion coefficient assumed to be constant. Both positive and negative tanks have identical dimensions, yielding an approximate volume of 100 mL. The initial liquid level in each tank is approximately 20 mm, corresponding to an initial electrolyte volume of around 20 mL per tank. The total vanadium ion concentration is 1.5 mol/L. Electrolyte is an average valence state of 3.5. Electrolyte compositions contain 1.5 M vanadium and 3 M H₂SO₄. Fresh electrolyte includes 20 mL of 1.5 M V²⁺/V³⁺ for anolyte and 20 mL of 1.5 M VO²⁺/VO₂ for catholyte. Before the charging/discharging cycle test, several prior cycles are performed to fully mix the cathode and anode electrolytes. Subsequently, the VRB is discharging to the cut-off voltage. V²⁺ is completely converted to V³⁺ in analyte, and VO₂⁺ is completely converted to VO²⁺ in the catholyte. Thus, the initial SOC of VRB is 0 %. Electrolyte circulation between the stack and reservoirs is driven by peristaltic pumps, with flow rates ranging from 1 mL/min to

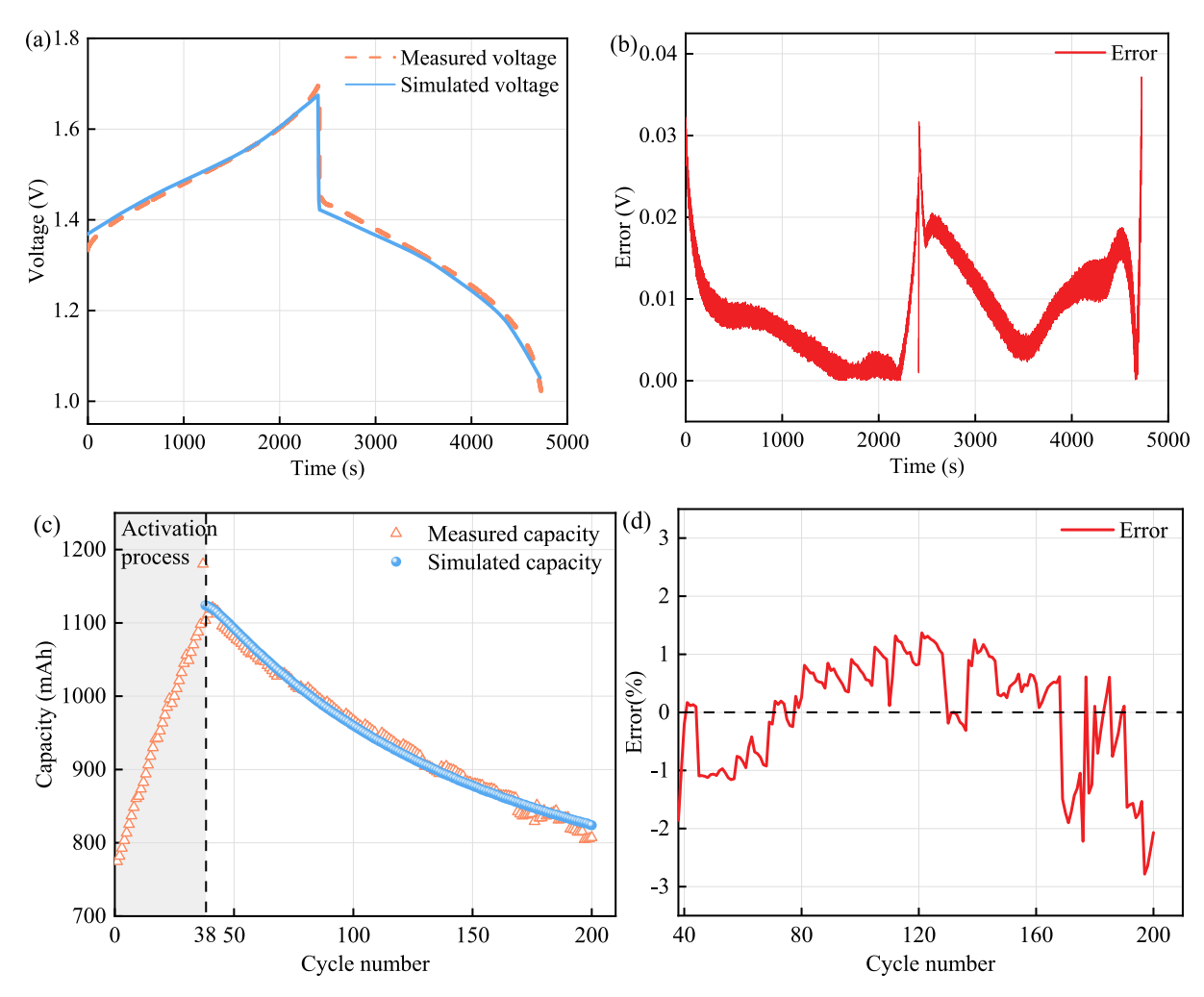


Fig. 5. Model validation results. (a) Stack voltage profile; (b) Voltage prediction error; (c) Available capacity vs. cycle number; (d) Capacity error vs. cycle number.

 $500~\rm mL/min$. It is commonly assumed in the research community that the pump control system provides sufficiently accurate and reliable flow regulation for experimental purposes. The cycle protocol requires the battery to be charged to $1.7~\rm V$ at a constant current of $1.8~\rm A$, followed by discharge to $1.0~\rm V$ at the same current magnitude. This charge-discharge process is repeated for a total of $200~\rm cycles$.

The proposed model was implemented in MATLAB 2023a using the parameters provided in Table 2 [17,34,36,41] to investigate the effect of different control strategies on VRB performance.

Fig. 5(a) compares the measured and estimated voltages over a full charge-discharge cycle at a constant current of 1.8 A. Fig. 5(b) shows the voltage error between simulation and experiment, with a maximum error of less than 0.04 V. Fig. 5(c) shows the comparison of available capacity over 200 cycles, while Fig. 5(d) presents the corresponding capacity error, which is within 3 %, occurring near the end of the test period. These results indicate that the proposed model closely aligns with the experimental observations and accurately captures the dynamic behavior of the VRB.

As seen in Fig. 5(c), an increase in battery capacity is observed during the initial cycles (1st-38th), a phenomenon commonly referred to as the battery activation process. This behavior can be attributed to the following factors:

- 1) Active species in the electrolyte are initially not fully activated and require several charge-discharge cycles to reach the full active states.
- 2) The porous carbon felt inside the cell is not completely wetted by the electrolyte, limiting the effective electrochemical reaction area.

3) The PEM is not fully wetted by the electrolyte, and the proton transport channels are not yet fully activated, resulting in reduced conductivity and incomplete electrochemical reactions of the active species.

Such activation behavior is typical in new or long-idled VRBs. To avoid misinterpretation of capacity trends, only data from cycles 38 to 200 are used for subsequent capacity analysis.

It should be noted that the simulation does not incorporate the short-term hydration/swelling behavior characteristic of Nafion membranes, which accounts for the rapid initial stabilization of electrolyte volume observed experimentally within the first 5–10 cycles [42]. The model reflects the longer-term cumulative effects of ion transport and water crossover, resulting in a slower exponential stability.

Fig. 6(a) presents photographic records of positive and negative electrolyte volumetric levels over 200 charge-discharge cycles. Fig. 6(b) shows the measured and simulated variations in electrolyte volume, while Fig. 6(c) presents the corresponding volume error. Excluding the activation stage, the error does not exceed approximately 3 % of the total electrolyte volume. Overall, the simulation results closely match the experimental data in terms of voltage, available capacity, and electrolyte volume variation on both sides, thereby validating the accuracy and reliability of the proposed model.

5. Results and discussion

In VRB systems, the traditional and most widely used strategy employs a constant, appropriately sized flow rate. To mitigate electrolyte

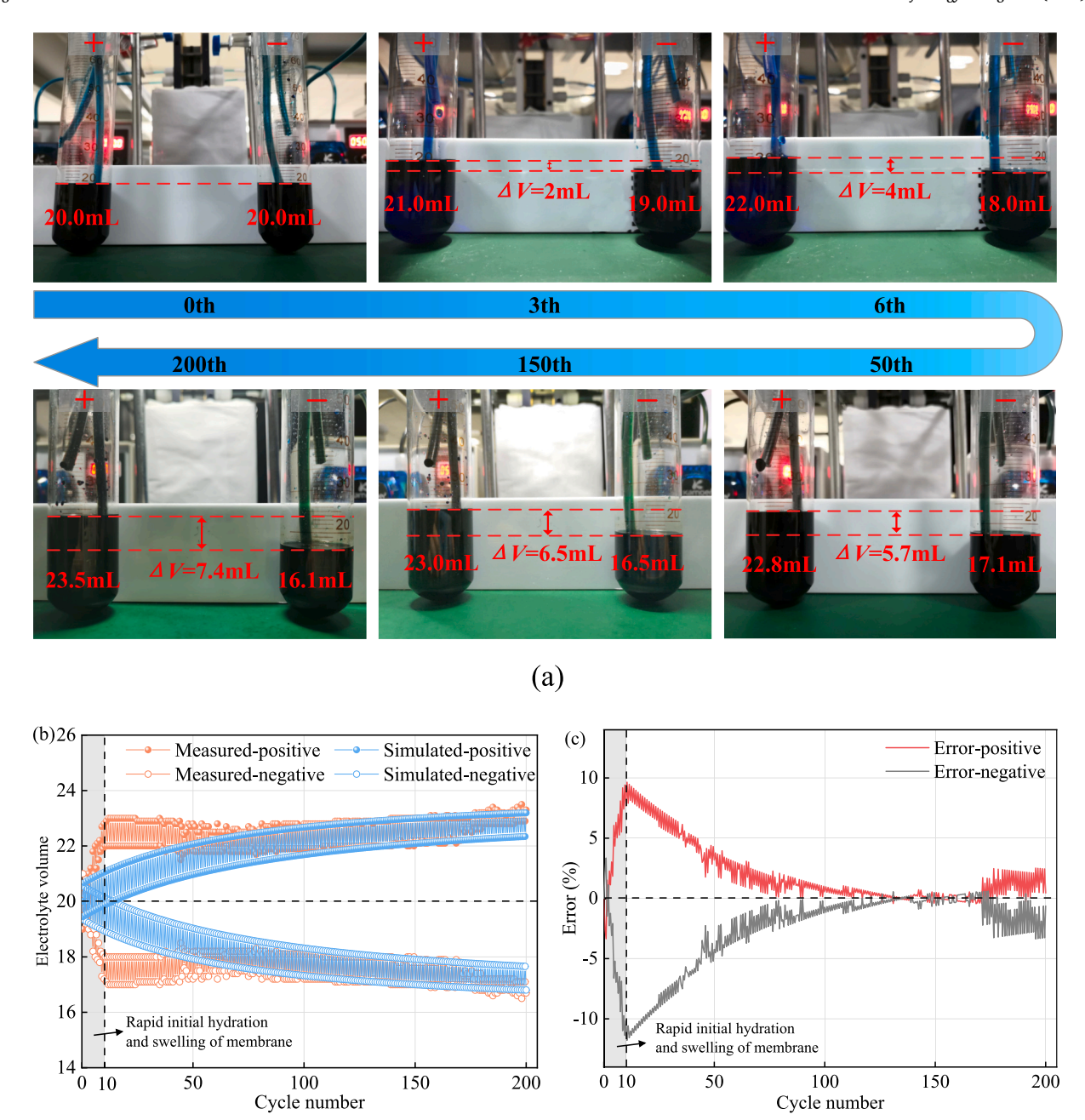


Fig. 6. Long-term experimental results. (a) Photographic records of electrolyte volume levels at the end of discharging; (b) Comparison of measured and simulated electrolyte volumes in the positive and negative tanks; (c) Electrolyte volume prediction error between measured and simulated data.

Table 3Comparison of flow rate settings used in the traditional CF and proposed AVF control strategies.

Strategy	Flow rate settings		
CF with FF λ_1 (traditional)	FF λ_1 (traditional) $Q_p = Q_n = \lambda_1 \cdot Q_{ ext{the}} = \lambda_1 \cdot \frac{I}{z F c_V}$		
AVF with FF λ_2 and $\xi_{\rm opt}$	$\begin{cases} Q_n = \lambda_2 \cdot Q_{\text{the}} = \begin{cases} \lambda_2 \cdot \frac{I}{zFc_V(1 - \text{SOC})}, & \text{charging} \\ \lambda_2 \cdot \frac{I}{zFc_V \text{SOC}}, & \text{discharging} \end{cases}$		
(Proposed)	$Q_p = \xi_{opt} \cdot Q_n = \begin{cases} \xi_{opt} \cdot \lambda_2 \cdot \frac{I}{zFc_V(1 - SOC)}, & \text{charging} \\ \xi_{opt} \cdot \lambda_2 \cdot \frac{IN}{zFc_VSOC}, & \text{discharging} \end{cases}$		

volume migration, the paper introduces an asymmetric flow rate control strategy. Table 3 presents the mathematical descriptions of the traditional CF strategy with FF λ_1 and the proposed AVF strategy with λ_2 and ξ_{opt} .

5.1. Determination of λ_{opt} and ξ_{opt}

The simulation protocol is identical to the experimental setup: Each cycle involves charging at 1.8 A until the stack voltage reaches a cutover voltage of 1.7 V, followed by discharging at 1.8 A down to a cutoff voltage of 1.0 V. A total of 200 cycles are simulated, during which different flow rate control strategies are applied across repeated trials to determine $\lambda_{\rm opt}$ and $\xi_{\rm opt}$.

To determine $\xi_{\rm opt}$, it is necessary first to obtain $\lambda_{\rm opt}$. As described in *Step 1.3* of the proposed control framework presented in Section 3.2, four performance metrics (CE, VE, EE, and SE) are evaluated at the

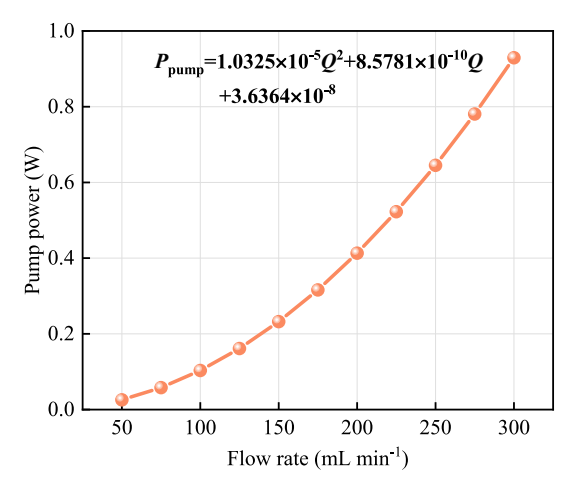


Fig. 7. Relationship between pump power consumption and flow rate.

Table 4Calculated pump power varies at different SOC intervals under CF and VF strategies during discharge.

Strategy	SOC	Flow rate (mL/min)	P_{pump} (W)
CF with FF λ_1	(0,1)	$6.58\lambda_1$	$P_{\text{pump}}(6.58\lambda_1)$
VF with FF λ_2	(0,0.1)	$65.84\lambda_2$	$P_{\text{pump}}(65.84\lambda_2)$
	(0.1, 0.2)	$32.92\lambda_{2}$	$P_{\text{pump}}(32.92\lambda_2)$
	(0.2,0.3)	$21.95\lambda_{2}$	$P_{\text{pump}}(21.95\lambda_2)$
	(0.3, 0.4)	$16.46\lambda_2$	$P_{\text{pump}}(16.46\lambda_2)$
	(0.4, 0.5)	$13.17\lambda_{2}$	$P_{\text{pump}}(13.17\lambda_2)$
	(0.5, 0.6)	$10.97\lambda_{2}$	$P_{\text{pump}}(10.97\lambda_2)$
	(0.6, 0.7)	$9.41\lambda_2$	$P_{\text{pump}}(9.41\lambda_2)$
	(0.7,0.8)	$8.23\lambda_2$	$P_{\text{pump}}(8.23\lambda_2)$
	(0.8, 0.9)	$7.32\lambda_2$	$P_{\text{pump}}(7.32\lambda_2)$
	(0.9,1.0)	$6.58\lambda_2$	$P_{\text{pump}}(6.58\lambda_2)$

200th cycle to assess system performance after long-term cycling. Among the four performance metrics, SE is particularly influenced by pump power losses, which depend on the total pressure drop, flow rate, and pump characteristics. As a result, SE provides the most accurate reflection of the practical performance of the VRB system, and it is thus selected as the primary evaluation metric. Fig. 7 shows the relationship between pump power and flow rate. Based on (35) and (36), Table 4 presents the variation of pump power with SOC under both CF and VF strategies during discharging. The resulting optimal FF $\lambda_{1,\rm opt}$ for the CF strategy and the $\lambda_{2,\rm opt}$ for the AVF strategy are compared in Fig. 8.

Fig. 8(a) illustrates the four performance metrics under the CF

strategies for various values of λ . The maximum SE of 0.6953 is achieved when $\lambda_{1,\text{opt}}=2$. Beyond this point, further increasing λ leads to a significant rise in pump power consumption, causing SE to decrease when $\lambda=3$. Similarly, Fig. 8(b) illustrates the corresponding efficiency metrics under the AVF strategy for different λ_2 values. The highest SE of 0.7302 is observed at $\lambda_{2,\text{opt}}=7$. The observed results are in agreement with recent findings reported in [17–19].

In theory, $\xi_{\rm opt}$ could be achieved by continuously adjusting pump-controlled flow rates. However, frequently starting and stopping the pumps can lead to mechanical wear and reduced operational lifespan. To balance performance with hardware longevity, we adopt a near-optimal control scheme with minimal switching. Specifically, *Step 2.5* of the control framework presented in Section 3.2 is modified by investigating specific $\xi_{\rm opt}$ at n discrete operating points corresponding to ${\rm SOC}_i=i/n$, where i=0,1,2,...,n. The local asymmetric coefficient, ξ_i , is calculated by

$$\xi_i = \frac{f_p(\mathrm{SOC}_i)}{f_n(\mathrm{SOC}_i)}, \quad \mathrm{SOC}_i = i \bigg/ n, \quad i = 0, 1, 2, \cdots, n \tag{42}$$

As an illustrative example, Fig. 9 shows the relationship between $\xi_{\rm opt}$ and ξ_i for n=10. A well-designed control strategy should meet the following criteria:

1) The operating points should "switch" between different ξ_i curves;

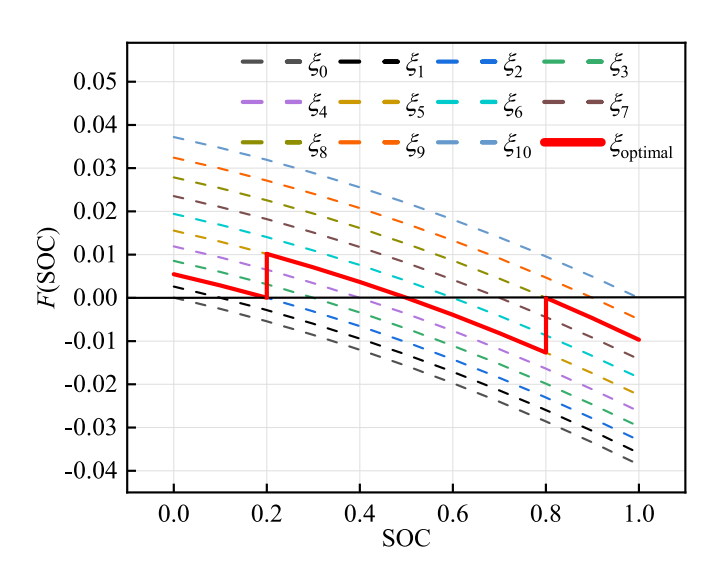


Fig. 9. Relationship between discontinuous ξ_{opt} and $\xi_0 - \xi_{10}$.

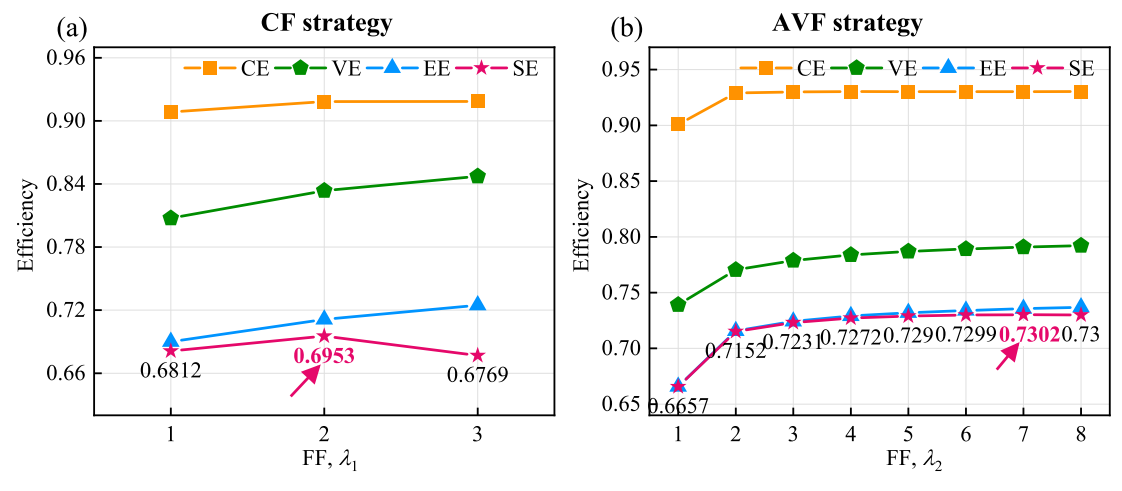


Fig. 8. Simulated results of CE, VE, EE, and SE at the 200th cycle under different flow rate factors λ. (a) CF strategy; (b) AVF strategy.

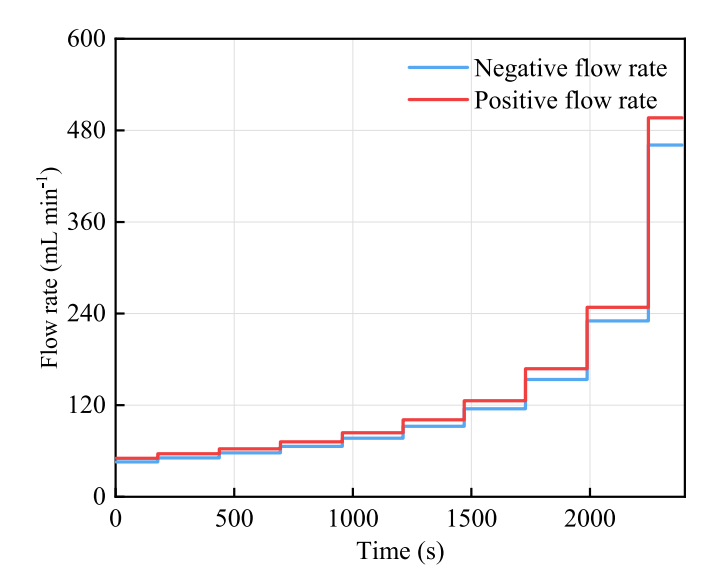


Fig. 10. Optimal flow rate control strategy during discharging based on discontinuous $\xi_{\rm opt}$.

Table 5Pump power varies with SOC under CF and AVF strategies during discharging.

- FF		0	
Strategy	SOC	Flow rate (mL/ min)	P _{pump} (W)
CF with FF $\lambda_1 = 2$	(0,1)	$Q_n = Q_p = 13.16$	0.0018
AVF with FF $\lambda_2 = 7$ and ξ_{opt} (Proposed)	(0,0.1)	$Q_n = 460.88$ $Q_p = 496.53$	2.3693
•	(0.1,0.2)		0.5923
	(0.2,0.3)	T	0.2672
	(0.3,0.4)	I .	0.1502
	(0.4,0.5)	$Q_n = 92.19$	0.0962
	(0.5,0.6)		0.0667
	(0.6,0.7)		0.0491
	(0.7,0.8)	$Q_p = 71.92$ $Q_n = 57.61$	0.0376
	(0.8,0.9)	$Q_p = 62.9$ $Q_n = 51.24$	0.0301
	(0.9,1.0)	$Q_p = 56.57$ $Q_n = 46.06$	0.0243
		$Q_p = 50.85$	

- 2) The operating points must remain close to the F(SOC) = 0 line;
- 3) The number of switches should be minimized.

A heuristic scheme that satisfies is also depicted in Fig. 9 and mathematically described by

$$\xi_{\text{opt}} = \begin{cases} \xi_2 = 1.0393, 0 < \text{SOC} < 0.2\\ \xi_5 = 1.0918, 0.2 \le \text{SOC} \le 0.8\\ \xi_8 = 1.0774, 0.8 < \text{SOC} < 1 \end{cases}$$
(43)

where only two switching points are required to cover the entire SOC range. Using $\lambda_{\rm opt}$ and this modified discontinuous $\xi_{\rm opt}$, the resulting AVF control strategy is obtained and illustrated in Fig. 10.

Table 5 lists the corresponding pump power as a function of SOC under both CF and AVF strategies during discharge. The total pump power in the AVF strategy is calculated as the average of the pump powers on the positive and negative sides.

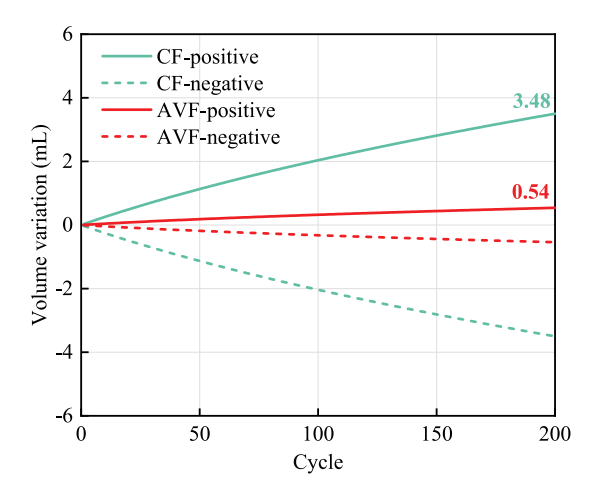


Fig. 11. Variation of positive and negative electrolyte volumes over 200 cycles for the CF strategy and the proposed AVF strategy, measured after each discharge process.

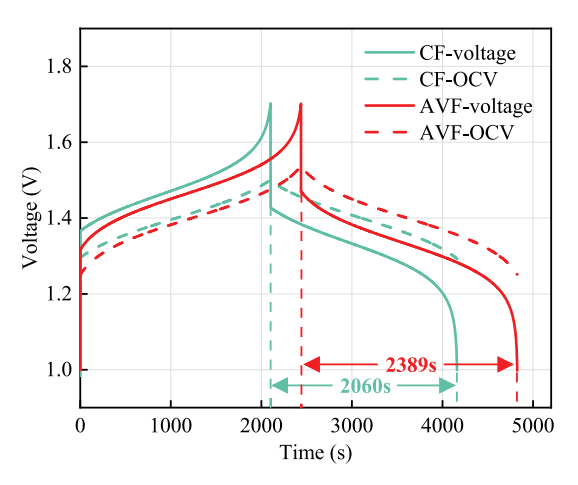


Fig. 12. Stack voltage and OCV profiles during the first charge-discharge cycle under the traditional CF strategy and the proposed AVF strategy.

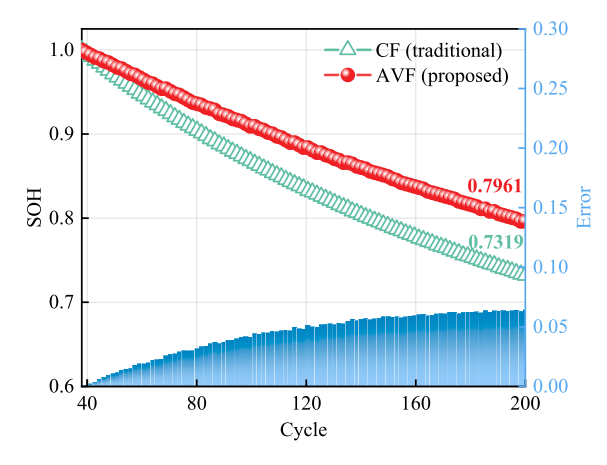


Fig. 13. Comparison of the SOH of the VRB under CF and AVF strategies during a 163-cycle charge-discharge test.

5.2. Comparison of electrolyte volume migration

This section presents an analysis of the impact of electrolyte volume migration under the CF and AVF strategies. Fig. 11 shows the evolution of electrolyte volumes in the positive and negative tanks over

Table 6 Flow rate settings for ACF1 and ACF2 strategies.

Strategy	Flow rate settings	
ACF1 with ξ_5 (Song et al. [31])	$\left\{egin{aligned} Q_n = Q_{ ext{the}} = rac{I}{zFc_V} \ Q_p = \xi_5{\cdot}Q_{ ext{the}} = \xi_5rac{I}{zFc_V} \end{aligned} ight.$	
ACF2 with $\xi = 1.28$ (Fetyan et al. [32])	$\left\{ egin{aligned} Q_n = Q_{ ext{the}} = rac{I}{zFc_V} \ Q_p = \xi \cdot Q_{ ext{the}} = 1.28 imes rac{I}{zFc_V} \end{aligned} ight.$	

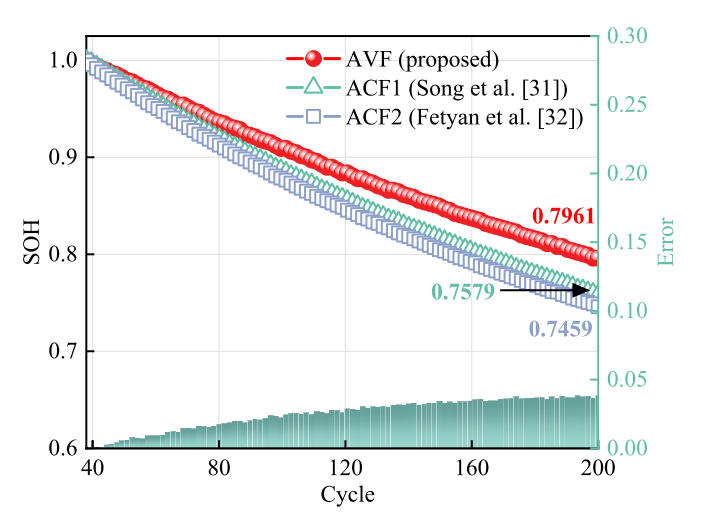


Fig. 14. Comparison of VRB capacity under the proposed AVF strategy, the ACF1 strategy by Song et al. [31], and the ACF1 strategy by Fetyan et al. [32].

continuous charge-discharge cycling. The results reveal a gradual increase in positive electrolyte volume and a decrease in negative electrolyte volume, mainly driven by viscosity differences during operation. In long-term operation, the reduction in the negative electrolyte volume can affect the battery capacity in the negative half-cell.

The volume transfer ratios (VTRs) of the positive and negative electrolytes are introduced here to quantify the volume changes during cycling. They are defined as follows:

$$VTR_p = \frac{V_p^t - V_{initial}}{V_{initial}}$$
 (44)

$$VTR_n = -VTR_n \tag{45}$$

where VTR_p and VTR_n represent the VTRs of the positive and negative electrolytes, respectively, V_p^t denotes the electrolyte volume in the positive tank, and V_{initial} is the initial electrolyte volume in each tank.

Fig. 11 illustrates the variation in electrolyte volume after each discharge process over 200 cycles for both the CF and AVF strategies, showing the positive and negative changes. It can be seen that after 200 charge/discharge cycles, the proposed AVF strategy resulted in only 0.54 mL increase in positive electrolyte volume, representing an 84.48 % reduction compared to the 3.48 mL increase observed in the CF strategy. In addition, the positive volume transfer ratio VTR_p for the AVF strategy is 2.7 %, indicating a 14.7 % decrease compared to the CF strategy. These results clearly demonstrate the effectiveness of the proposed AVF strategy in reducing electrolyte volume variation.

5.3. Comparison of stack voltage and open-circuit voltage

This section assesses the impact of ξ_{opt} on battery performance by analyzing stack voltage and OCV, as derived from (1) and (2). Fig. 12

presents the stack voltage $U_{\rm stack}$ and OCV during the first cycle for both the CF and AVF strategies. The results indicate that the AVF strategy leads to extended charging and discharging times compared to the CF strategy. While OCV provides a baseline estimate of electrochemical potential, it does not account for overpotentials arising from ohmic resistance, activation, and concentration effects. As such, $U_{\rm stack}$ delivers a more accurate representation of actual operating conditions. The discharging time increased from 2060 s under the CF strategy to 2389 s with the AVF strategy, which corresponds to a 13.77 % increase in discharging capacity based on the ampere-hour integration method. Results demonstrate that adopting the optimized parameter $\xi_{\rm oPt}$ effectively enhances the battery's charge-discharge performance.

5.4. Comparison of battery SOH

Side reactions during charge-discharge cycling induce ion migration of the negative electrolyte toward the positive side, resulting in a volume imbalance. This imbalance impairs the performance of the negative half-cell and contributes to the decay of both battery capacity and SOH. Fig. 13 presents the SOH decay trends and associated errors for the traditional CF strategy and the proposed AVF strategy over 163 consecutive cycles. The blue bars, corresponding to the right y-axis, indicate the difference in capacity delay between the two strategies. By the 200th cycle, the SOH of the AVF strategy decayed to 0.7961, compared to 0.7319 for the CF strategy, with a maximum error of 0.0642. These results confirm that the proposed AVF strategy effectively alleviates capacity degradation. Compared to the CF strategy, $\xi_{\rm opt}$ enabled a 6.42 % reduction in SOH degradation after 163 charging/discharging cycles, which contributes to a significant improvement in overall battery performance.

5.5. Comparison of different asymmetrical flow-rate strategies

Two state-of-the-art asymmetric flow rate strategies [31,32], denoted as ACF1 and ACF2, are compared with the proposed AVF strategy. In the ACF1 strategy, FF is neglected, and electrolyte viscosity is assumed to remain constant at different SOCs, fixed at the value corresponding to 50 % SOC. Consequently, the asymmetric coefficient is set to ξ_5 . Similarly, the ACF2 strategy also does not account for FF and adopts fixed positive and negative flow rates at a ratio of 36:28, yielding an asymmetrical coefficient of $\xi=1.28$. Mathematical descriptions of the ACF1 and ACF2 strategies are provided in Table 6.

Fig. 14 illustrates the capacity degradation trends for the AVF, ACF1, and ACF2 strategies. It can be observed that the proposed AVF strategy outperforms the two existing asymmetrical strategies with constant flow. Specifically, it demonstrates a 3.82 % less capacity degradation than the ACF1 strategy and a 5.02 % less than the ACF2. The blue bar at the bottom of the figure indicates the capacity differences between the AVF and the ACF1 strategies, with a maximum deviation of 0.038 observed at the 200th cycle.

In contrast, the proposed AVF strategy is designed based on the underlying electrolyte migration mechanism, explicitly accounting for both the FF and viscosity variations at different SOCs. By adaptively regulating the flow rate, the AVF strategy effectively slows down the rate of capacity degradation and ultimately achieves superior capacity retention compared to the two ACF strategies. These results provide direct evidence of the improved performance and effectiveness of the proposed AVF strategy.

6. Conclusion

Traditional flow rate control strategies for vanadium redox flow batteries (VRBs) typically maintain the electrolyte flow rates on the positive and negative sides in a symmetric manner, overlooking the long-term effects of these imbalances on the electrolyte. To enhance operational efficiency and extend battery lifespan, we introduce an asymmetric flow control strategy that optimally adjusts the electrolyte flow rates based on transport dynamics. Based on Darcy's law, this approach determines the optimal flow rate ratio in order to mitigate electrolyte migration and minimize capacity degradation. Compared with the traditional strategy, the simulation results show that the SE has increased by 3.49 %. Experimental validation demonstrates that the proposed strategy can reduce electrolyte volume variation by 84.48 % and decrease the volume transfer ratio of the positive electrolyte by 14.7 % compared to traditional methods. Furthermore, after 163 cycles, the strategy achieves a 6.42 % reduction in state-of-health decay compared to the traditional strategy and at least a 3.82 % enhancement in capacity retention compared to existing asymmetric flow rate strategies. Results demonstrate its potential to significantly improve VRB performance, both in terms of efficiency and capacity retention.

It should be pointed out that the experimental measurement of the pressure drop and various flow rate strategies will be prioritized in future work to further validate and refine the proposed model. Meantime, incorporating membrane hydration dynamics and short-term swelling effects into the model would further improve the consistency between experimental observations and simulations.

CRediT authorship contribution statement

Shaojin Wang: Writing – original draft, Visualization, Validation, Methodology, Investigation, Conceptualization. Yana Zhou: Writing – review & editing, Validation. Yang Li: Writing – review & editing, Supervision, Conceptualization. Chengyan Li: Writing – review & editing, Data curation. Xifeng Lin: Methodology. Xinan Zhang: Software. Binyu Xiong: Writing – review & editing, Supervision, Investigation, Funding acquisition.

Declaration of competing interest

The authors declare that they have no known competing financial interests or personal relationships that could have appeared to influence the work reported in this paper.

Acknowledgments

This work is supported by the National Natural Science Foundation of China (No. 52177221).

Data availability

Data will be made available on request.

References

- [1] Z. Huang, A. Mu, L. Wu, B. Yang, Y. Qian, J. Wang, Comprehensive analysis of critical issues in all-vanadium redox flow battery, ACS Sustain. Chem. Eng. 10 (2022) 7786–7810, https://doi.org/10.1021/acssuschemeng.2c01372.
- [2] T. Ouyang, M. Zhang, P. Qin, X. Tan, Flow battery energy storage system for microgrid peak shaving based on predictive control algorithm, Appl. Energy 356 (2024) 122448, https://doi.org/10.1016/j.apenergy.2023.122448.
- [3] S. Bogdanov, M. Pugach, S. Parsegov, V. Vlasov, F.M. Ibanez, K.J. Stevenson, et al., Dynamic modeling of vanadium redox flow batteries: practical approaches, their applications and limitations, J. Energy Storage 57 (2023) 106191, https://doi.org/ 10.1016/i.est.2022.106191.
- [4] G. Yang, Y. Zhu, Z. Hao, Y. Lu, Q. Zhao, K. Zhang, et al., Organic electroactive materials for aqueous redox flow batteries, Adv. Mater. 35 (2023), https://doi.org/ 10.1002/adma.202301898.
- [5] Z. Huang, A. Mu, L. Wu, H. Wang, Vanadium redox flow batteries: flow field design and flow rate optimization, J. Energy Storage 45 (2022) 103526, https://doi.org/ 10.1016/j.est.2021.103526.
- [6] Y. Chen, P. Xiong, S. Xiao, Y. Zhu, S. Peng, G. He, Ion conductive mechanisms and redox flow battery applications of polybenzimidazole-based membranes, Energy Storage Mater. 45 (2022) 595–617, https://doi.org/10.1016/j.ensm.2021.12.012.
- [7] B. Xiong, Y. Li, Y. Ding, J. Wang, Z. Wei, J. Zhao, et al., Numerical analysis of vanadium redox flow batteries considering electrode deformation under various flow fields, J. Power Sources 564 (2023) 232814, https://doi.org/10.1016/j. jpowsour.2023.232814.

- [8] J. Kim, H. Park, Recent advances in porous electrodes for vanadium redox flow batteries in grid-scale energy storage systems: a mass transfer perspective, J. Power Sources 545 (2022) 231904, https://doi.org/10.1016/j.jpowsour.2022.231904.
- H. Chen, M. Cheng, X. Feng, Y. Chen, F. Chen, J. Xu, Analysis and optimization for multi-stack vanadium flow battery module incorporating electrode permeability, J. Power Sources 515 (2021) 230606, https://doi.org/10.1016/j. incurr 2021 232606
- [10] S. Wang, Y. Li, C. Li, X. Lin, W. Ma, N. Tong, et al., A systematic study of pipe and electrical connections for multi-stack vanadium redox flow battery modules considering electrolyte transport delays, Chem. Eng. J. 519 (2025) 164929, https://doi.org/10.1016/j.cei.2025.164929.
- [11] A. Hussain, A. Mehmood, A. Saleem, M.K. Majeed, W. Raza, R. Iqbal, et al., Polyetherimide membrane with tunable porous morphology for safe lithium metalbased batteries, Chem. Eng. J. 453 (2023) 139804, https://doi.org/10.1016/j. cei.2022.139804.
- [12] Z. Yu, X. Jia, Y. Cai, R. Su, Q. Zhu, T. Zhao, et al., Electrolyte engineering for efficient and stable vanadium redox flow batteries, Energy Storage Mater. 69 (2024) 103404, https://doi.org/10.1016/j.ensm.2024.103404.
- [13] B. Sziffer, M.J. Mayer, V. Józsa, Detailed system modeling of a vanadium redox flow battery operating at various geographical locations, Appl. Energy 384 (2025) 125473, https://doi.org/10.1016/j.apenergy.2025.125473.
- [14] J. Ren, Y. Li, Z. Wang, J. Sun, Q. Yue, X. Fan, et al., Thermal issues of vanadium redox flow batteries, Int. J. Heat Mass Transf. 203 (2023) 123818, https://doi.org/ 10.1016/j.ijheatmasstransfer.2022.123818.
- [15] P. Jienkulsawad, T. Jirabovornwisut, Y.-S. Chen, A. Arpornwichanop, Improving the performance of an all-vanadium redox flow battery under imbalance conditions: online dynamic optimization approach, ACS Sustain. Chem. Eng. 8 (2020) 13610–13622, https://doi.org/10.1021/acssuschemeng.0c02973.
- [16] X. Ma, H. Zhang, C. Sun, Y. Zou, T. Zhang, An optimal strategy of electrolyte flow rate for vanadium redox flow battery, J. Power Sources 203 (2012) 153–158, https://doi.org/10.1016/j.jpowsour.2011.11.036.
- [17] A. Tang, J. Bao, M. Skyllas-Kazacos, Studies on pressure losses and flow rate optimization in vanadium redox flow battery, J. Power Sources 248 (2014) 154–162. https://doi.org/10.1016/j.jpowsour.2013.09.071.
- [18] M. Guarnieri, A. Trovò, F. Picano, Enhancing the efficiency of kW-class vanadium redox flow batteries by flow factor modulation: an experimental method, Appl. Energy 262 (2020) 114532, https://doi.org/10.1016/j.apenergy.2020.114532.
- [19] A. Morozov, M. Pugach, A. Polyakov, P. Osinenko, A. Bolychev, V. Terzija, et al., Optimal flow factor determination in vanadium redox flow battery control, IEEE Access 12 (2024) 19277–19284, https://doi.org/10.1109/ACCESS.2024.3361830.
- [20] B. Xiong, J. Tang, Y. Li, C. Xie, Z. Wang, X. Zhang, et al., Design of a two-stage control strategy of vanadium redox flow battery energy storage systems for grid application, IEEE Trans. Sustain. Energy 13 (2022) 2079–2091, https://doi.org/ 10.1109/TSTE.2022.3181751.
- [21] P. Jienkulsawad, T. Jirabovornwisut, Y.-S. Chen, A. Arpornwichanop, Effect of battery material and operation on dynamic performance of a vanadium redox flow battery under electrolyte imbalance conditions, ENERGY 268 (2023) 126708, https://doi.org/10.1016/j.energy.2023.126708.
- [22] W. Chen, J. Kang, Optimization of electrolyte flow and vanadium ions conversion by utilizing variable porosity electrodes in vanadium redox flow batteries, Chem. Phys. 529 (2020) 110577, https://doi.org/10.1016/j.chemphys.2019.110577.
- [23] J. Shan, D. Xiao, Uncovering the effect of ion exchange membrane on capacity decay and efficiency for all-vanadium redox flow battery by modeling analysis, Int. J. Green Energy 19 (2022) 1367–1374, https://doi.org/10.1080/ 1545075.2071.1007752.
- [24] L. Yan, D. Li, S. Li, Z. Xu, J. Dong, W. Jing, et al., Balancing osmotic pressure of electrolytes for nanoporous membrane vanadium redox flow battery with a draw solute, ACS Appl. Mater. Interfaces 8 (2016) 35289–35297, https://doi.org/ 10.1021/acsami.6b12068.
- [25] W. Duan, B. Li, D. Lu, X. Wei, Z. Nie, V. Murugesan, et al., Towards an all-vanadium redox flow battery with higher theoretical volumetric capacities by utilizing the VO2+/V3+ couple, J. Energy Chem. 27 (2018) 1381–1385, https://doi.org/10.1016/j.jechem.2018.05.020.
- [26] M.Y. Lu, W.W. Yang, Y.M. Deng, W.Z. Li, Q. Xu, Y.L. He, Mitigating capacity decay and improving charge-discharge performance of a vanadium redox flow battery with asymmetric operating conditions, Electrochim. Acta 309 (2019) 283–299, https://doi.org/10.1016/j.electacta.2019.04.032.
- [27] F. Toja, L. Perlini, D. Facchi, A. Casalegno, M. Zago, Dramatic mitigation of capacity decay and volume variation in vanadium redox flow batteries through modified preparation of electrolytes, Appl. Energy 354 (2024) 122262, https://doi. org/10.1016/j.apenergy.2023.122262.
- [28] Z. Wang, Z. Guo, J. Ren, Y. Li, B. Liu, X. Fan, et al., An electrolyte with elevated average valence for suppressing the capacity decay of vanadium redox flow batteries, ACS Cent. Sci. 9 (2023) 56–63, https://doi.org/10.1021/ acscentsci.2c01112.
- [29] E. Agar, A. Benjamin, C.R. Dennison, D. Chen, M.A. Hickner, E.C. Kumbur, Reducing capacity fade in vanadium redox flow batteries by altering charging and discharging currents, J. Power Sources 246 (2014) 767–774, https://doi.org/ 10.1016/j.jpowsour.2013.08.023.
- [30] K.W. Knehr, E.C. Kumbur, Role of convection and related effects on species crossover and capacity loss in vanadium redox flow batteries, Electrochem. Commun. 23 (2012) 76–79, https://doi.org/10.1016/j.elecom.2012.07.008.
- [31] Y. Song, X. Li, J. Xiong, L. Yang, G. Pan, C. Yan, et al., Electrolyte transfer mechanism and optimization strategy for vanadium flow batteries adopting a Nafion membrane, J. Power Sources 449 (2020) 227503, https://doi.org/10.1016/ j.jpowsour.2019.227503.

- [32] A. Fetyan, M.O. Bamgbopa, A. Andisetiawan, A. Alhammadi, R.A. Susantyoko, Evaluation of asymmetric flow rates for better performance vanadium redox flow battery, Batteries Supercaps 6 (2023), https://doi.org/10.1002/batt.202300301.
- [33] B. Xiong, J. Tang, Y. Li, P. Zhou, S. Zhang, X. Zhang, et al., A flow-rate-aware data-driven model of vanadium redox flow battery based on gated recurrent unit neural network, J. Energy Storage 74 (2023) 109537, https://doi.org/10.1016/j.est.2023.109537.
- [34] R. Xiong, B. Xiong, Q. Zhang, S. Shi, Y. Su, D. Zhang, Capacity fading model of vanadium redox flow battery considering water molecules migration, Int. J. Green Energy 19 (2022) 1613–1622, https://doi.org/10.1080/15435075.2021.2015599.
- [35] A.A. Shah, H. Al-Fetlawi, F.C. Walsh, Dynamic modelling of hydrogen evolution effects in the all-vanadium redox flow battery, Electrochim. Acta 55 (2010) 1125–1139, https://doi.org/10.1016/j.electacta.2009.10.022.
- [36] W.-J. Zou, Y.-B. Kim, S. Jung, Capacity fade prediction for vanadium redox flow batteries during long-term operations, Appl. Energy 356 (2024) 122329, https:// doi.org/10.1016/j.apenergy.2023.122329.
- [37] D. Jeong, S. Jung, Numerical analysis of cycling performance of vanadium redox flow battery, Int. J. Energy Res. 44 (2020) 5209–5222, https://doi.org/10.1002/ er 5261

- [38] C. Sun, J. Chen, H. Zhang, X. Han, Q. Luo, Investigations on transfer of water and vanadium ions across Nafion membrane in an operating vanadium redox flow battery, J. Power Sources 195 (2010) 890–897, https://doi.org/10.1016/j. jpowsour.2009.08.041.
- [39] T. Ma, Z. Huang, X. Xie, B. Li, Evaluation of the effect of hydrogen evolution reaction on the performance of all-vanadium redox flow batteries, Electrochim. Acta 504 (2024) 144895, https://doi.org/10.1016/j.electacta.2024.144895.
- [40] Q. Xu, T.S. Zhao, C. Zhang, Effects of SOC-dependent electrolyte viscosity on performance of vanadium redox flow batteries, Appl. Energy 130 (2014) 139–147, https://doi.org/10.1016/j.apenergy.2014.05.034.
- [41] X. Ma, H. Zhang, F. Xing, A three-dimensional model for negative half cell of the vanadium redox flow battery, Electrochim. Acta 58 (2011) 238–246, https://doi. org/10.1016/j.electacta.2011.09.042.
- [42] J. Sun, X. Li, X. Xi, Q. Lai, T. Liu, H. Zhang, The transfer behavior of different ions across anion and cation exchange membranes under vanadium flow battery medium, J. Power Sources 271 (2014) 1–7, https://doi.org/10.1016/j. jpowsour.2014.07.111.